1 August 2000

ELSEVIER

Optics Communications 182 (2000) 25–34

OPTICS COMMUNICATIONS

www.elsevier.com/locate/optcom

Spatial coherence characterization of undulator radiation

Chang Chang [a,b,*], Patrick Naulleau [a], Erik Anderson [a], David Attwood [a,b]

[a] *Center for X-Ray Optics, Lawrence Berkeley National Laboratory, Berkeley, CA 94720, USA*
[b] *Department of Electrical Engineering & Computer Science, University of California, Berkeley, CA 94720, USA*

Received 12 April 2000; accepted 8 June 2000

Abstract

The coherence properties of undulator radiation at extreme ultraviolet (EUV) wavelengths are measured using the Thompson–Wolf two-pinhole method. The effects of asymmetric source size and beamline apertures are observed. High spatial coherence EUV radiation is demonstrated. Projection of these same capabilities to the x-ray region is straightforward. Published by Elsevier Science B.V.

1. Introduction

Coherent radiation offers important opportunities for both science and technology. The well defined phase relationships characteristic of coherent radiation, allow for diffraction-limited focusing (as in scanning microscopy), set angular limits on diffraction (as in protein crystallography), and enable the convenient recording of interference patterns (as in interferometry and holography). While coherent radiation has been readily available and widely utilized at visible wavelengths for many years [1–5], it is just becoming available for wide use at shorter wavelengths [6]. This is of great interest as the shorter wavelengths, from the extreme ultraviolet (EUV, 10–20 nm wavelength), soft x-ray (1–10 nm), and x-ray (< 1 nm) regions of the spectrum, correspond to photon energies that are well matched to the primary electronic resonances (K-shell, L-shell, etc.) of essentially all elements, thus providing a powerful combination of techniques for the elemental and chemical analysis of physical and biological materials at very high spatial resolution. Tunable, coherent radiation in these spectral regions is available primarily due to the advent of undulator radiation at modern synchrotron facilities [7–12], where relativistic electron beams of small cross-section transverse periodic magnet structures, radiating very bright, powerful, and spatially coherent radiation at short wavelengths. Recent progress with EUV lasers [13], high laser harmonics [14,15], and free electron lasers [16] may soon add to these capabilities. In this paper we utilize the classic two-pinhole diffraction technique [2], an extension of Young's two-slit interference experiment [1], to simply and accurately characterize the degree of spatial coherence provided by undulator radiation. We show that, with the aid of modest pinhole spatial filtering, undulator radiation can provide tunable short wavelength radiation with a very high degree of spatial coherence at presently available user facilities. Spatially coherent power of

* Corresponding author. Fax: +1-510-486-6103; e-mail: cnchang@lbl.gov

0030-4018/00/$ - see front matter. Published by Elsevier Science B.V.
PII: S0030-4018(00)00811-7

order 30 mW is available in the EUV [17], and is expected to scale linearly with wavelength to about 0.3 mW in the hard x-ray region [6].

For radiation with a high degree of coherence and a well-defined propagation direction, it is convenient to describe coherence properties in longitudinal and transverse directions. For a source of diameter d, emission half-angle θ, and full spectral bandwidth $\Delta\lambda$ at wavelength λ, relationships for full spatial coherence and longitudinal coherence length, l_{coh}, are given respectively by

$$d \cdot \theta = \lambda/2\pi \tag{1}$$

and

$$l_{\mathrm{coh}} = \lambda^2/2\Delta\lambda, \tag{2}$$

where d, θ, and $\Delta\lambda$ are $1/\sqrt{e}$ measures of Gaussian distributions. Based on measures of the source size and theoretical predictions of the emission angle, it is estimated that undulator radiation, as discussed in this paper, emanating from an electron beam of highly elliptical cross-section, will approach full spatial coherence Eq. (1) in the vertical plane, while being coherent over only a fraction of the radiated beam in the horizontal direction. Here we present a detailed characterization of an undulator beamline optimized for operation in the EUV regime [17].

Undulator beamline 12.0 at Lawrence Berkeley National Laboratory's Advanced Light Source (ALS) was developed to support high-accuracy wave-front interferometry of EUV optical systems [18,19]. With an electron beam of elliptical cross-section, having a vertical size $d_v = 2\sigma_v = 32$ μm, and an emission half-angle $\theta = 80$ μrad (the central radiation cone containing a $1/N$ relative spectral bandwidth, where N is the number of magnet periods of the undulator [6].), the product $d \cdot \theta$ is just slightly larger (20%) than $\lambda/2\pi$ at the 13.4 nm wavelength used in these experiments. Thus we expect to see strongly correlated fields, of high spatial coherence, in the vertical plane. The horizontal beam size is considerably larger with $d_h = 2\sigma_h = 520$ μm, so that with approximately the same emission half-angle we expect it to be spatially coherent over only a fraction of the horizontal extent of the radiated beam.

The coherence characterization presented here is performed at the focus of the condenser system used to re-image the undulator source to the entrance of our experimental chamber. In the case of beamline 12, this condenser is a Kirkpatrick–Baez (KB) system [6]. Its focal plane serves as the entrance plane for various experiments, including EUV phase-shifting point diffraction interferometry [18,19]. The coherence measurement is based on an implementation, at a shorter wavelength, of the well known Thompson and Wolf two-pinhole experiment [2]. The Thompson and Wolf experiment is essentially an extension of Young's classic two-slit interference experiment [1], where in this case fringe visibility is recorded as a function of pinhole separation in order to determine the spatial coherence properties of the illuminating beam. Under the conditions that: (1) the pinholes are small enough such that the field within each pinhole can be regarded as constant, (2) the bandwidth of the illuminating beam is narrow enough that temporal coherence does not significantly affect fringe visibility, and (3) the intensity at the two sampled points are equal, the fringe visibility can be shown to be proportional to the magnitude of the complex coherence factor, μ, [3,4]. Typical measured interference patterns are presented in Fig. 2, which shows interference modulation of the Airy envelope as a function of pinhole separation distance. These patterns provide a direct measure of the spatial coherence of undulator radiation as transported by the beamline optical system.

2. Experiment

The experimental system is depicted in Fig. 1. The beamline [17] provides an overall 60:1 demagnified image of the source in the focal plane of the KB system. The undulator employed at this beamline has a magnet period (λ_u) of 8 cm, 55 magnet periods (N), and a non-dimensional magnetic field parameter $K = 2.7$. The electron beam energy is 1.9 GeV, with a corresponding relativistic Lorentz factor $\gamma = 3720$. The acceptance half-angle (NA) of undulator radiation for these experiments is set by the acceptance aperture of the beamline, which is a 1.6 mm diameter circle placed 16.7 meters downstream of the undulator exit. This acceptance NA of 48 μrad is somewhat smaller than the central radiation cone

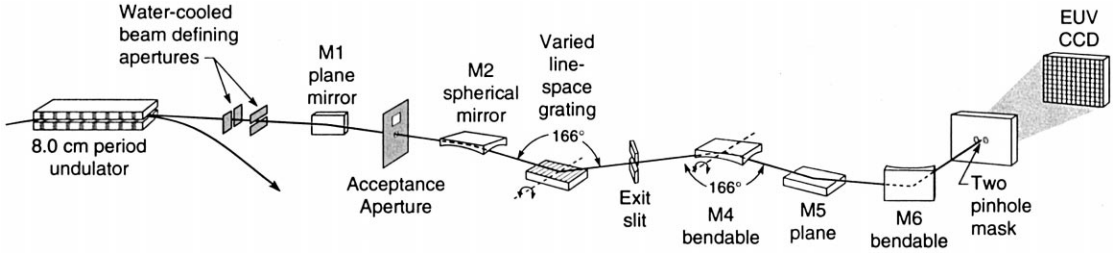

Fig. 1. The experiment setup shows the undulator, beamline optics, monochromator grating and exit-slit, Kirkpatrick–Baez (KB) re-focusing optics (M4 and M6), and the spatial coherence measuring end-station consisting of a two-pinhole mask and an CCD electronic array detector. The two pinholes are shown here with a horizontal separation; vertical separation tests are also employed.

half-angle, $\theta_{cen} = \sqrt{1 + K^2/2}\,/\,\gamma\sqrt{N} = 80$ μrad [6,17]. The radiation within θ_{cen} has a natural bandwidth of $\lambda/\Delta\lambda = N$, corresponding to a longitudinal coherence length, l_{coh}, of 0.37 μm. The monochromator bandpass of this beamline can be narrowed to values as large as $\lambda/\Delta\lambda = 1100$, by adjusting the size of its horizontal exit-slit. Except where stated otherwise, all experiments reported in this paper were performed with the monochromator exit-slit set such as to pass the entire $\lambda/\Delta\lambda = 55$ natural undulator bandwidth. Accounting for the 48 μrad acceptance NA, the spatially coherent power is expected to be about 12 mW, within a relative bandwidth of $\lambda/\Delta\lambda = 55$ at $\lambda = 13.4$ nm [17]. Using the full 80 μrad acceptance NA defined by θ_{cen} would yield expected coherent power of 30 mW. This bandwidth is sufficient to assure that the quasi-monochromatic condition required for this experiment is satisfied, i.e. that the temporal coherence does not significantly affect fringe visibility.

As shown in Fig. 1, the M2 spherical mirror images the undulator output vertically to the monochromator exit-slit. The calculated FWHM of the vertical intensity profile on the exit-slit is 17 μm, neglecting aberrations on M2 mirror. The KB system is composed of two asymmetric, bendable reflective mirrors (M4 and M6). Mirror M6 directly demagnifies the undulator source in the horizontal direction by a factor of 60, whereas M4 demagnifies the monochromator exit-slit in the vertical direction by a factor of 7.2. M2 and M4 together provide a total vertical demagnification of 60 in the plane of the two-pinhole mask.

To implement these coherence tests, a patterned mask containing multiple 450 nm-diameter-pinhole pairs, with separations ranging from 1 to 9 μm, was placed in the vicinity of the KB system focus, i.e. at the demagnified image of the undulator source. The 450 nm pinhole diameter is chosen to be significantly smaller than the expected coherence width, while providing reasonable throughput and appropriate working distance for full Airy pattern recording at the charge-coupled-device (CCD) electronic array detector. The mask, fabricated using electron-beam lithography and reactive-ion etching, consists of a 360 nm-thick Ni absorbing layer evaporated on a 100 nm-thick Si_3N_4 membrane. The mask features are etched completely through the membrane prior to the Ni evaporation, leaving the pinholes completely open in the finished mask. Pinhole circularity and size are confirmed by observing the resultant far field Airy patterns, as recorded on an the CCD.

The pinhole array mask is mounted on an x–y–z stage, allowing desired pinhole separations to be selected sequentially, and the coherence to be studied as a function of focal position. A back-thinned, back-illuminated, EUV sensitive CCD camera is placed 26 cm downstream of the mask to record the resulting interference pattern. The active area of the CCD is 25.4 mm × 25.4 mm, in a 1024 by 1024 pixel array. Typical exposure times for a recorded pattern vary between 50 ms and 5 s depending on pinhole separation, storage ring current, and beamline apertures.

Because the divergence created by the pinhole diffraction is large relative to the pinhole separation, the two diffraction patterns overlap to a high degree on the CCD. In order to determine the magnitude of the complex coherence factor, μ, from the fringe visibility, we must know the relative intensities of

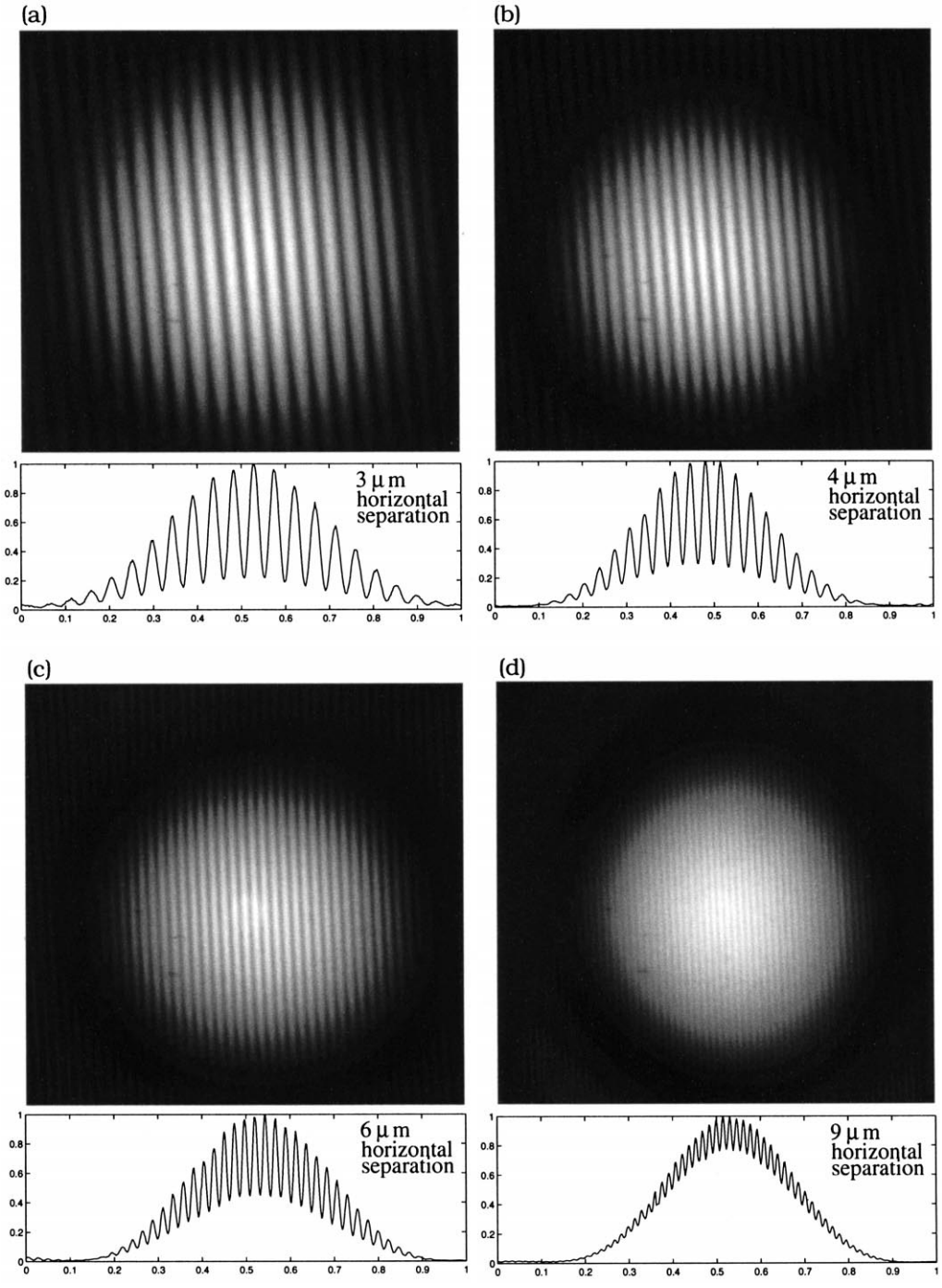

Fig. 2. Measured two-pinhole interference patterns for horizontal pinhole separations of 3, 4, 6 and 9 μm, for a wavelength of 13.4 nm and a beamline acceptance half-angle of 48 μrad. The pinhole diffraction patterns overlap and produce an interference pattern within the Airy envelope. The interference patterns are recorded on an EUV sensitive CCD camera, located 26 cm downstream of the pinhole mask. Pinhole diameter range from 400 to 500 nm, but are equal in their respective pairs. As shown in the lineouts, fringe visibility of the modulation decreases for larger separations. Spectral resolution for these measurements is 55.

the illuminating beam at the two pinholes or, alternatively, guarantee them to be equal. This can be challenging as the pinholes are near the KB focal plane, where the beam is small and may display

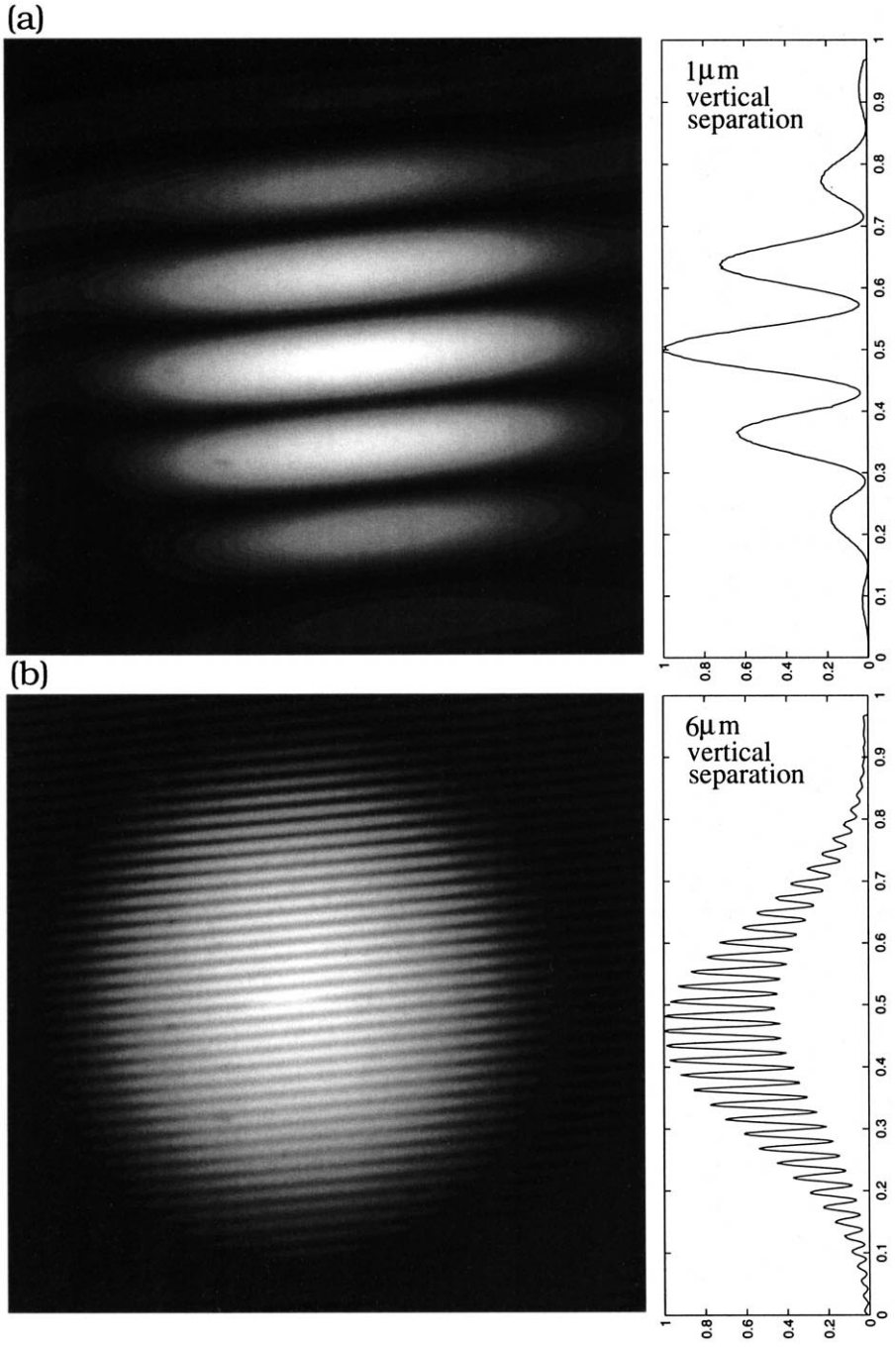

Fig. 3. Measured two-pinhole interference patterns for vertical pinhole separations of 1 and 6 μm, a wavelength of 13.4 nm, and an acceptance half-angle of 48 μrad.

structure due to aberrations in the optics. Because it is impractical to independently measure the intensity at each pinhole, we attempt to guarantee the equal intensity condition by performing a large ensemble (greater than 50) of measurements for each pinhole separation, intentionally displacing the pinhole pair relative to the incident beam. Because beam-intensity non-uniformity can only degrade fringe visibility, we take the highest fringe visibility from the ensemble of measurements as representing the coherence-limited fringe visibility.

Fig. 2 shows the recorded interference patterns for horizontal pinhole separations of 3, 4, 6 and 9 μm. The measured magnitude of the fringe visibility decreases with larger pinhole separation as expected. Fig. 3 shows several interference patterns obtained with vertically displaced pinhole pairs. Fringe modulation is generally better than that of horizontally displaced pinholes. In order to verify our ability to control and measure the beamline coherence properties, the measurement was repeated at a larger beamline acceptance NA. This NA can be controlled by way of the acceptance aperture described above. The measured spatial coherence decreases in both directions as expected when the 48 μrad acceptance aperture is replaced by a larger aperture allowing the entire 80 μrad central radiation cone to pass.

The interference pattern at the CCD can be written as [4]

$$I(x,y) = 2I^{(1)}(x,y)\left[1 + \mu\cos\left(\frac{2\pi}{\lambda z}sx + \phi\right)\right], \tag{3}$$

where $I^{(1)}(x,y)$ is the Airy intensity envelope in the recording plane due to pinhole diffraction, x is the axis on the recording plane that is parallel to the pinhole separation, s is the pinhole separation, λ is the wavelength, and z is the distance from the pinholes to the recording plane. Note that the phase ϕ describes the fringe shift relative to the geometric center of the interference pattern. With equi-phase illumination of the two pinholes and proper pinhole alignment, $\phi = 0$. Because fringe visibility is defined as

$$\mathscr{V} \equiv \frac{I_{\max} - I_{\min}}{I_{\max} + I_{\min}}, \tag{4}$$

we have $\mathscr{V} = \mu$ as a constant over the entire interferogram for the cases considered here.

To obtain the fringe visibility from the interference pattern, we perform a two-dimensional Fourier transform of the interferogram and separate the ze-

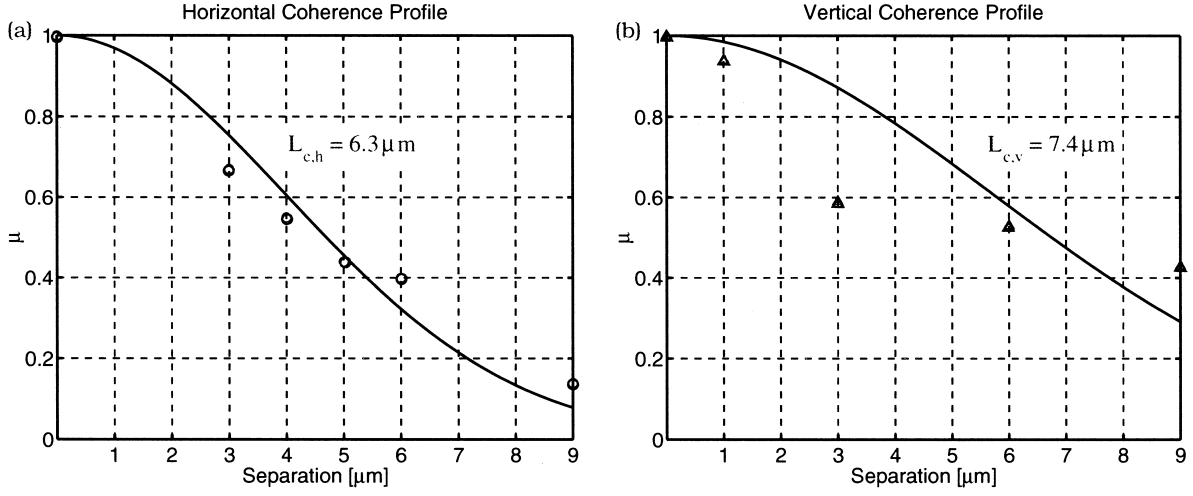

Fig. 4. The measured coherence factor μ as function of pinhole separation distance for (a), horizontally and (b), vertically separated pinholes. For these measurements, a 48 μrad half-angle acceptance aperture is used. The measured spatial coherence distance decreases with larger pinhole separations as expected. Larger uncertainty in the vertical 3 μm separation may be due to a smaller number of interferograms collected in this case. The data points are fitted to a Gaussian curve in each case.

roth order and the two first-order peaks. As seen in Eq. (3), the Fourier transform of the interferogram $I(x,y)$ can be represented as the convolution of the Fourier transform of the Airy envelope with three delta functions. The delta functions arising from the $1+\cos(\cdot)$ term can be written as

$$\delta(f_x,f_y)+\frac{\mu}{2}\left[\delta\left(f_x+\frac{s}{\lambda z},f_y\right)+\delta\left(f_x-\frac{s}{\lambda z},f_y\right)\right].$$

Furthermore, the Fourier transform of the Airy envelope becomes the autocorrelation of the pinhole. The resultant pattern in the frequency domain is therefore one zeroth order peak and two symmetric first-order peaks, each properly scaled. Ideally, the fringe visibility is two times the relative strength of the first-order peak to the zeroth-order peak. In practice, we apply properly displaced top-hat filters centered at each peak and integrate within the filters. The fringe visibility is then determined by two times the ratio of the integration under the first-order peak to that under the zeroth-order peak.

In Fig. 4 we show μ as a function of pinhole separation for both horizontally and vertically separated pinholes. One observes that the transverse coherence distance in the vertical plane is greater than that in the horizontal plane, for this 48 μrad acceptance NA. Following the convention in [4], a transverse coherence distance L_c for the measured coherence profiles (Fig. 4) is obtained by determining the width of an equivalent top-hat function, i.e.,

$$L_c \equiv \int_{-\infty}^{\infty} |\mu(\Delta x)|^2 \mathrm{d}\Delta x. \tag{5}$$

The measured transverse coherence distance in the horizontal direction, $L_{c,h}$, is found to be approximately 6.3 μm and the measured transverse coherence distance in the vertical direction, $L_{c,v}$, is found to be approximately 7.4 μm. This is due to the fact that the vertical source dimension is sub-resolution in size at this acceptance angle, while the horizontal

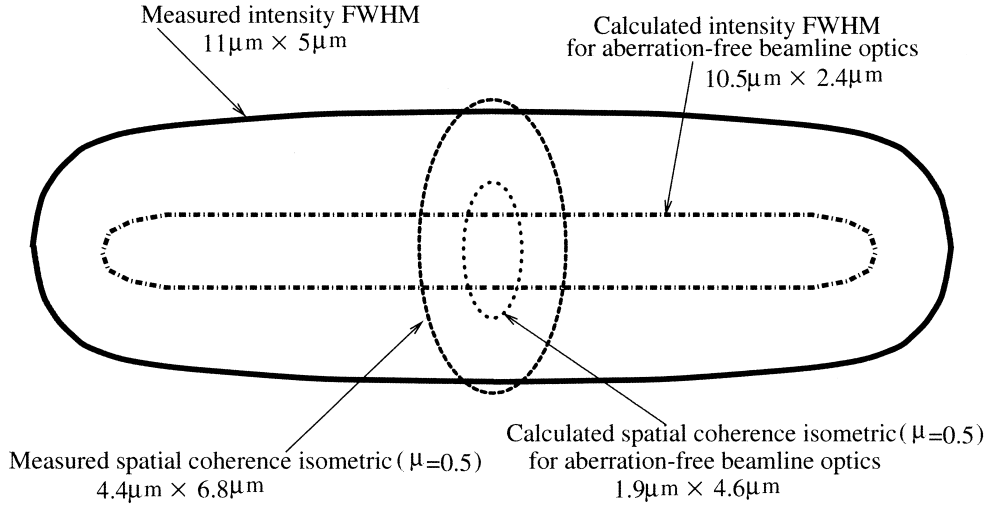

Fig. 5. The beamline is designed to image the undulator output to the KB focus with a demagnification of 60 and an acceptance half-angle of 48 μrad. The undulator output in this calculation is assumed to be a monochromatic ($\lambda = 13.4$ nm), spatially incoherent Gaussian-shaped source with $(\sigma_x,\sigma_y) = (260\ \mu\mathrm{m}, 16\ \mu\mathrm{m})$ [6], corresponding to source plane values of 612 μm × 38 μm FWHM. The solid line shows the FWHM of the measured KB focal intensity distribution. The dash-dot line is the FWHM of this calculated KB focal intensity distribution assuming an aberration-free beamline. The intensity distribution FWHM values are increased by aberrations from ideal values of 10.5 μm(H) × 2.4 μm(V), to experimental values of 11 μm(H) × 5 μm(V). The dashed line represents the calculated focal plane spatial coherence isometric ($\mu = 0.5$) for experimental values of wavelength, acceptance NA, and demagnification, as calculated using the van Cittert–Zernike theorem [3,4]. The asymmetric coherence isometric is due to the asymmetry of the source intensity distribution.

size is not [1]. After propagating from the undulator exit (source), the FWHM of the spatial coherence profile, as calculated by the van Cittert–Zernike theorem, is 0.3 mm(H) × 5.2 mm(V) at the beamline acceptance aperture. Therefore, the spatial coherence profile at the KB focal plane (image plane) is expected to be asymmetric with vertical coherence better than horizontal coherence.

The effect of radiation directly transmitted through the mask membrane, a source of noise in these measurements, can be seen in Fig. 2(d). This effect becomes more significant as the pinhole separation increases because the limited beam size (see Fig. 5) results in a reduced illumination intensity at each pinhole, whereas the directly transmitted radiation remains fixed. This directly transmitted light adds a background noise to the interference pattern, thus reducing fringe visibility locally in the affected region. Therefore, when applying the Fourier transform method to the cases of large pinhole separations, we avoid the region containing directly transmitted light. This Fourier transform method has the advantage of evaluating the fringe visibility as an integrated, rather than localized, property of the full interferogram.

The intensity and coherence distribution in the KB focal plane is calculated by way of computer simulation for an aberration-free beamline. The simulation shows that the coherence profile is wider than the calculated intensity profile for the aberration-free beam in the vertical direction, which means that without aberrations the beam would be essentially fully coherent in the vertical direction. Horizontally, the coherence profile is dominated by the acceptance NA. As described above, this asymmetry is expected based on the geometry of the system.

Fig. 5 displays both FWHM intensity contours and $\mu = 0.5$ isometrics for both the aberration-free simulation case, and the actual measured results. In both cases the vertical coherence is seen to be larger than the beam vertical FWHM, indicating nearly complete coherence in the vertical direction. Also both simulation and experiment show the horizontal coherence to be smaller than the vertical coherence and significantly smaller than the beam. This is a result of the extended source in the horizontal direction and the beamline geometry. The results differ, however, in that the measured coherence and beam-size are larger than those predicted for the aberration-free simulation. The beam-size increase is attributed to aberrations in the KB. By comparing the two intensity profiles we surmise the aberration limited point-spread function of the KB to be about 4 μm in diameter. We assume these aberrations to also play a role in the increased coherence observed experimentally.

2.1. Effect of monochromator exit-slit

The natural bandwidth of undulator radiation within the central radiation cone, θ_{cen}, is set by the number of magnet periods N, which is 55 in these experiments. The monochromator is designed to transmit a bandpass variable from $\lambda/\Delta\lambda = 55$ to 1100. The larger value is useful in experiments requiring a longer coherence length (to 7.4 μm at 13.4 nm wavelength). These values of spectral bandpass correspond to exit-slit widths of 320 μm and 16 μm, respectively. Exit-slit size greater than 320 μm does not further affect the monochromator bandpass. All data presented to this point correspond to a 400 μm exit-slit size ($\lambda/\Delta\lambda = 55$). Use of a smaller monochromator exit-slit narrows the transmitted spectrum, but also has the effect of decreasing the transmitted beam's transverse phase-space, and thus increasing the spatial coherence length in the vertical plane. To study the effect of the monochromator exit-slit size, we have repeated the experiment with exit-slit size as a parameter. Fig. 6 shows the measured horizontal and vertical coherence as a function of monochromator exit-slit size. For a vertical pinhole separation of 6 μm, the fringe visibility varies from 0.38 to 0.94 as the exit-slit size changes from 400 μm to 50 μm. For the horizontally oriented 4 μm separation pinholes, the fringe visibility varies from 0.47 to 0.60 as the exit-slit size changes from

[1] Simple analysis of a critical illumination system like the one considered here would suggest the coherence to be symmetric when the NA is symmetric. More detailed analysis reveals, however, that the small vertical source size causes the vertical coherence width at the entrance pupil to be large relative to the pupil size. In this case we violate the assumptions typically used for predicting coherence in a critical illumination. This causes a preferential increase of coherence in the vertical direction.

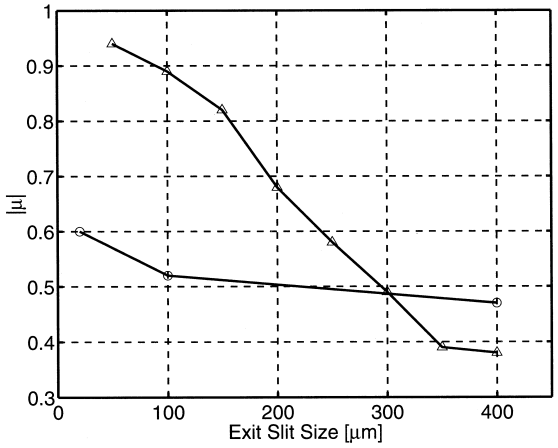

Fig. 6. The vertical opening of monochromator's exit-slit has significant effect on the vertical coherence but not on the horizontal coherence. A smaller exit-slit size decreases the vertical phase-space of the transmitted radiation, thus increasing the vertical coherence. Horizontal coherence is relatively unaffected. This is done with a larger beamline acceptance NA.

400 μm to 20 μm. As one expects, the exit-slit also acts as a spatial filter, having a significant effect on spatial coherence in the vertical plane, and minimal effect in the horizontal plane.

2.2. Wave-front null test

The two-pinhole experiment presented here can also be used to measure the departure from sphericity of the pinhole-diffracted wave. Fig. 7 is derived from the measured interference pattern obtained with 450 μm diameter pinholes horizontally placed 9 μm apart. To determine the underlying wave-front quality of the two nearly spherical waves used to produce the interference pattern, the interferogram is analyzed using conventional Fourier-transform wave-front reconstruction techniques routinely applied to carrier-frequency interferograms [20]. The resulting wave-front is then compared to what one would expect from two perfectly spherical waves in our recording geometry. The rms departure from a sphere is taken to represent the underlying pinhole-diffracted wave-front quality. For example, at a numerical aperture of 0.025 (a typical input numerical aperture for testing EUV optics), the wave-front

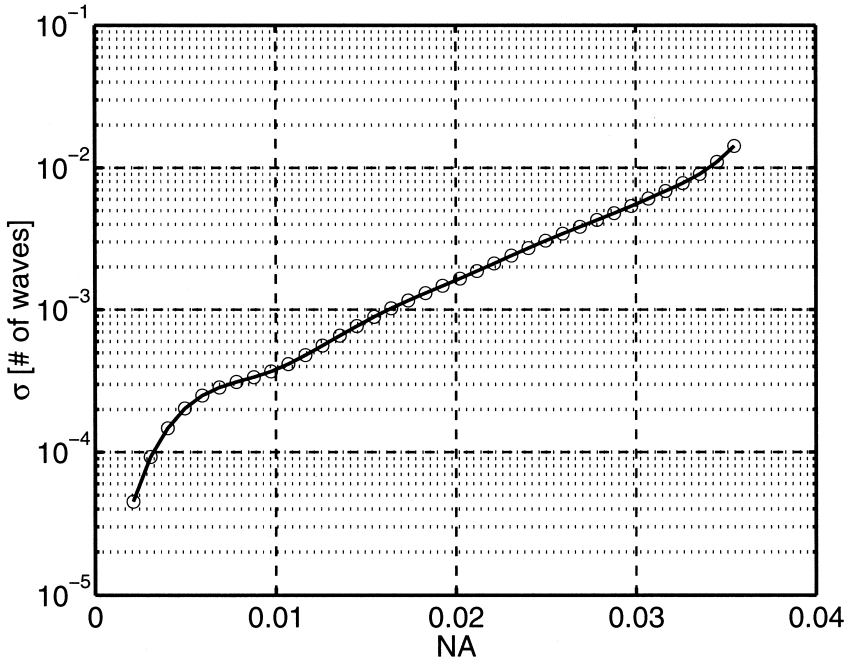

Fig. 7. Departure of pinhole generated wave-front from sphericity, expressed as an rms number of waves at $\lambda = 13.4$ nm. For example, the data indicates that with 450 nm-pinhole filtered radiation a wave-front departure from a sphericity of $\lambda/1000$ is obtained across a wave-front of about 0.016 NA (equal to 13 picometer rms at this wavelength and NA).

quality from these 450 μm pinholes is seen to be $\lambda/330$, exceeding current requirements for such tests [18,19].

3. Conclusion

The coherence properties of spatially filtered undulator radiation have been measured. A very high degree of spatial coherence is demonstrated, as expected on the basis of a simple model. The effect of an asymmetric source size on the resultant coherence properties is observed, and is consistent with aperturing within the beamline optical system used to transport radiation to the experimental chamber. Based on these observations and well understood scaling of undulator radiation, it is evident that high average power, spatially coherent radiation is available at modern storage rings with the use of appropriate pinhole spatial filtering techniques.

Acknowledgements

The authors would like to thank Dr. Kenneth Goldberg for valuable discussion. Special thanks are due to the entire CXRO engineering team and most notably to Phil Batson, Paul Denham, Drew Kemp and Gideon Jones for bringing the experimental hardware to fruition. This work was supported in part by the Office of Basic Energy Sciences, Department of Energy, by DARPA's Advanced Lithography Program, by the Air Force Office of Scientific Research, by Intel Corporation, and by the Extreme Ultraviolet Lithography Limited Liability Corporation.

References

[1] T. Young, Lectures on Natural Philosophy I, London, 1807, 464.
[2] B.J. Thompson, E. Wolf, J. Opt. Soc. Am.er. 47 (1957) 895.
[3] M. Born, E. Wolf, Principles of Optics., Cambridge University Press, Cambridge UK, 1999, seventh edition.
[4] J.W. Goodman, Statistical Optics.,Wiley, New York, 1985.
[5] N. Bloembergen, IEEE J. Quantum Electron. 20 (1984) 556.
[6] D.T. Attwood, Soft X-Rays and Extreme Ultraviolet Radiation., Cambridge University Press, Cambridge UK, 1999, chapters 5 and 8.
[7] D. Attwood, K. Halbach, K.-J Kim, Science 228 (1985) 1265.
[8] R. Coisson, Appl. Optics 34 (1995) 904.
[9] A. Kondratenko, A. Skrinsky, Opt. Spectrosc. 42 (1977) 189. While not specifically addressing undulator radiation, this paper points out the essence of spatially coherent radiation from relativistic electrons.
[10] Y. Takayama, R.Z. Tai, T. Hatano, T. Miyahara, W. Okamoto, Y. Kagoshima, J. Synchro. Radiat. 5 (1998) 456.
[11] D.L. Abernathy, G. Gruebel, S. Brauer, I. McNulty, G.B. Stephenson, S.G.J. Mochrie, A.R. Sandy, N. Mulders, M. Sutton, J. Synchro. Radiat. 5 (1998) 37.
[12] Z.H. Hu, P.A. Thomas, A. Snigirev, I. Snigireva, A. Souvorov, P.G.R. Smith, G.W. Ross, S. Teat, Nature 392 (1998) 690.
[13] M.C. Marconi, J.L.A. Chilla, C.H. Moreno, B.R. Benware, J.J. Rocca, Phys. Rev. Lett. 79 (1997) 2799.
[14] C. Spielmann, H. Burnett, R. Sartania, R. Koppitsch, M. Schnurer, C. Kan, M. Lenzner, P. Wobrauschek, F. Krausz, Science 278 (1998) 661.
[15] D. Schulze, M. Dorr, G. Sommerer, J. Ludwig, P.V. Nickles, T. Schlegel, W. Sandner, M. Drescher, U. Kleineberg, U. Heinzmann, Phys. Rev. A 57 (1998) 3003.
[16] A recent Nature News in Brief, 02 Mar. 2000, report describes the shortest wavelength FEL to date, <100 nm, achieved at the Deutsches Elektronen–Synchrotron (DESY) in Hamburg. The following review article describes preperation for those experiments: H. Nuhn, J. Rossbach, J. The challenge to be overcome to produce the ultimate x-ray source – the x-ray laser. Synchrotron Radiation News 13 (2000) 18.
[17] D. Attwood, P. Naulleau, K. Goldberg, E. Tejnil, C. Chang, R. Beguiristain, P. Batson, J. Bokor, E.M. Gullikson, M. Koike, H. Medecki, J.H. Underwood, IEEE J. Quantum Electron. 35 (1999) 709.
[18] P. Naulleau, K.A. Goldberg, S.H. Lee, C. Chang, D. Attwood, J. Bokor, Appl. Optics 38 (1999) 7252.
[19] K. Goldberg, P. Naulleau, J. Bokor, J. Vac. Sci. Technol. B 17 (1999) 2982.
[20] M. Takeda, H. Ina, S. Kobayyashi, J. Opt. Soc. Am. 72 (1982) 156.